Photoemission electron microscope for the study of magnetic materials

Simone Anders,[a] Howard A. Padmore, Robert M. Duarte, Timothy Renner, Thomas Stammler, and Andreas Scholl
Lawrence Berkeley National Laboratory, Berkeley, California 94720

Michael R. Scheinfein
Department of Physics and Astronomy, Arizona State University, Tempe, Arizona 85287-1504

Joachim Stöhr
IBM Research Division, Almaden Research Center, San Jose, California 95120

Laurent Séve and Boris Sinkovic
Department of Physics, University of Connecticut, Storrs, Connecticut 06269

(Received 15 March 1999; accepted for publication 14 June 1999)

The design of a high resolution photoemission electron microscope (PEEM) for the study of magnetic materials is described. PEEM is based on imaging the photoemitted (secondary) electrons from a sample irradiated by x rays. This microscope is permanently installed at the Advanced Light Source at a bending magnet that delivers linearly polarized, and left and right circularly polarized radiation in the soft x-ray range. The microscope can utilize several contrast mechanisms to study the surface and subsurface properties of materials. A wide range of contrast mechanisms can be utilized with this instrument to form topographical, elemental, chemical, magnetic circular and linear dichroism, and polarization contrast high resolution images. The electron optical properties of the microscope are described, and some first results are presented. © *1999 American Institute of Physics.* [S0034-6748(99)02910-X]

I. INTRODUCTION

Photoemission electron microscopy (PEEM) using ultraviolet (UV) radiation was first developed in the 1930's,[1,2] and has since developed into a well-established technique. The resolution of modern PEEM instruments approaches 10 nm, within a factor of two of the theoretical limit for uncorrected microscopes of 5 nm.[3,4] PEEM is similar to low energy electron microscopy (LEEM), a technique pioneered by the work of Bauer and his group,[5] that has rapidly developed over the last few years for the studies of thin film growth processes. The implementation of LEEM instruments has been instrumental in stimulating new developments for PEEM. The refinement of LEEM by Bauer[5] and the coupling of PEEM with synchrotron radiation by Tonner[6,7] has resulted in a resurgence of interest in this area over the past few years. This has led to the construction of PEEMs by several groups[6–12] as well as the introduction of commercial systems. Our motivation in developing the instrument reported here was to construct a system for spectromicroscopic imaging of magnetic surfaces near the theoretical resolution limit for this type of microscope. One key target was to achieve sufficient positional stability so that the theoretical resolution could be approached while acquiring spectroscopic data; as series of images are required, high stability over tens of minutes is needed. A second goal was to provide this high level of performance in a beamline and end station environment dedicated to microscopy; this was necessary to ensure a high level of productivity, and for the instrument to achieve a high level of maturity and sophistication. Finally, this system has enabled us to develop most of the electron optical building blocks for an aberration corrected microscope of even higher resolution.

In PEEM photons incident on a sample cause photoelectron emission if the energy of the photons is larger than the work function of the sample. These photoemitted electrons are extracted into an electron-optical imaging system by a large electric field that is applied between the sample and the first electrode of the electron optical system. This field is the first lens of the microscope. Several electron-optical lenses are used to form a full field image of the emitted electrons onto a detector such as a phosphor that converts electrons into visible light.

Two contrast mechanisms are available in UV-PEEM: topographical contrast and work function contrast. Topographical contrast is due to distortion of the electric field around surface topographical features. The field distribution distortions disturb the electron trajectories which produce image contrast. Work function contrast is manifest in the intensity modulation of the photoemission intensity due to the different emission probability in regions of different work function.

Additional imaging modes are available when x-ray photons are used to stimulate photoelectrons. Elemental contrast is achieved by tuning the incident x-ray wavelength through absorption edges of elements. X-ray absorption and the resulting photoelectron emission intensity is strongly enhanced at absorption edges. Areas on the surface containing the corresponding element emit more photoelectrons and thus appear bright in the PEEM image at a given absorption edge

[a]Electronic mail: sanders@lbl.gov

 © 1999 American Institute of Physics

x-ray energy. The fine structure in the energy dependence of the x-ray absorption can be characteristic of the chemical bonding state of surface atoms. Near edge x-ray absorption fine structure (NEXAFS) spectroscopy[13] can be applied to two-dimension image formation to obtain chemical contrast. Typically, images are acquired at several x-ray energies near a given absorption edge. The differences in these images can be used to detect local bonding characteristics at the surface. Elemental and chemical contrast has been utilized in PEEM studies of high T_c superconductors,[14] geological samples,[15] biological samples,[16] semiconductor materials,[17] computer hard disks[18] and sliders,[19] and polymer dewetting phenomena.[20]

Linearly and circularly polarized x rays can be used to study the orientation of molecules. In orientation contrast, linearly polarized x rays are strongly absorbed when the electrical vector of the light and the orientation of a bond in the molecule are parallel, and the absorption is weak for a perpendicular orientation.[21] This effect was first applied to x-ray microscopy by Smith and Ade[22] using a scanning x-ray transmission microscope (STXM) for studying the molecular orientation in Kevlar fibers. This contrast was also used to study molecular orientation of rubbed polymer thin films.[23,24] Furthermore, x-ray magnetic circular dichroism (XMCD) can be utilized to study magnetic materials[25] since the absorption of left and right handed circularly polarized radiation varies with the relative orientation of the magnetic moment in the sample. XMCD permits the determination of spin and orbital moments using sum rules,[26,27] and PEEM has been applied using XMCD contrast to study magnetic structures.[28–30] Finally, x-ray magnetic linear dichroism can be utilized to study the properties of antiferromagnetic materials. First attempts of antiferromagnetic imaging have been reported by Spanke *et al.*[31] for NiO(100) films.

Submicron magnetic structures and devices find application in the magnetic storage industry. Giant magnetoresistance (GMR) and colossal magnetoresistance (CMR) have stimulated growth in this area to such an extent that times between discovery and the production of a product have diminished to merely years. New magnetic device applications are numerous (e.g., magnetic random access memory). Technological progress here implies a reduction in size and an increase in complexity. Modern microscopy and analysis techniques commonly applied to the study of submicron magnetic structures include Kerr microscopy,[32,33] near-field magneto-optical imagine,[34,35] Lorentz microscopy,[36] scanning electron microscopy with polarization analysis,[37] (SEMPA) spin polarized low energy electron microscopy (SPLEEM),[38] and magnetic force microscopy (MFM).[39,40] Only transmission electron microscopy based techniques have a higher spatial resolution than PEEM. However, XMCD-PEEM can be used to simultaneously measure (without alteration of the material) the absolute magnetic moments with elemental and chemical specificity, submonolayer surface sensitivity, and the ability to probe several nanometers of material. This combination of spectroscopy with high resolution surface microscopy makes XMCD-PEEM one of the most powerful tools in the study of magnetic structures.

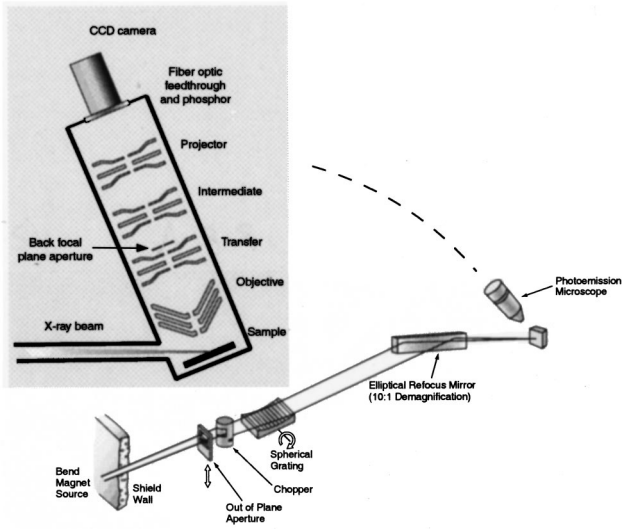

FIG. 1. Layout of beamline 7.3.1. at the Advanced Light Source and of the PEEM2 endstation.

A new PEEM has been designed that is dedicated to the study of magnetic materials and structures. We refer to this instrument as PEEM2 to indicate that it is our second generation PEEM. This article describes the electron optical properties of the PEEM, its construction and performance, and some initial results.

II. BEAMLINE AND PEEM2 LAYOUT

PEEM2 is installed at the bending magnet beamline 7.3.1 at the Advanced Light Source (ALS) in Berkeley. Figure 1 shows the optical layout of the beamline and PEEM2. The beamline was specifically designed for XMCD microscopy. The spherical grating monochromator is entrance slitless and delivers monochromatic radiation in the energy range of 175–1300 eV. Since the vertical source size at the center of this bending magnet is less than 30 μm and corresponds to the typical field of view of the microscope, the source can be directly imaged onto the sample at unity magnification. The low line density of the grating (200 lines/mm) leads to a very slow variation of the focal length with the wavelength, therefore the monochromator can work with a fixed imaging distance.[41] As the magnification of the PEEM determines the required field of view and hence illumination, the sample is placed in the monochromatic focal plane, without the use of exit slits as typical for conventional systems. This results in an energy dispersed vertical line. However, over the typical field of view of 30 μm the wavelength is essentially fixed. The energy dispersion is 1 eV/mm at 285 eV and 10 eV/mm at 800 eV. Considering the angle of incidence on the sample, this translates to an energy variation over the field of view (30 μm) of 10 meV at 285 eV and 100 meV at 800 eV. The horizontal source size in the ALS is approximately 300 μm full width at half maximum (FWHM), so to illuminate our required 30 μm field size and to maximize the flux density, a 10:1 horizontal demagnification is used. The maximum aperture that can be collected from the source is dictated by this required demagnification and the maximum convergence onto the sample. The maxi-

mum convergence itself is limited by the critical angle of reflection, i.e., the angle at which the x-ray reflectivity drops to zero. The critical angle of grazing incidence is a function of the photon energy and decreases as the energy increases; taking our maximum photon energy of 1300 eV, for a platinum or gold reflector, the critical angle is approximately 40 mrad. In theory the maximum convergence angle could be as high as the critical angle, but we conservatively take half this value. The 20 mrad convergence and the required demagnification of 10:1 define the source horizontal angular acceptance to be 2 mrad. In order to take such a large horizontal aperture and focus it to a small image, the value of geometrical aberrations must be carefully considered.

The photon flux is very high for a bending magnet beamline because the minimum number of optical components are used, and the field of view and spectral resolution are optimized for XMCD-PEEM. The photon flux is 3×10^{12} photon/s in a 30 μm spot when the storage ring is operated at 1.9 GeV with a ring current of 400 mA in a design bandpass of 1 eV at 1000 eV. A mask upstream from the monochromator (see Fig. 1) is used to select above plane (left circularly polarized), in plane (linearly polarized), or below plane (right circularly polarized) radiation. The resolving power of the beamline is $E/\Delta E=1800$.

The angle between the sample surface and the incident x-ray beam is 30°. The microscope optical axis is oriented at an angle of 90° with respect to the electric field vector of the radiation for linearly polarized light.

The objective lens of PEEM2 is an electrostatic tetrode lens with a stigmator/deflector assembly located in its back focal plane. A transfer lens produces a 1:1 image and a second objective back focal plane outside the lens where an aperture is located. Four different apertures are mounted on a small flexure stage and can be easily exchanged in vacuum (2 mm, 50 μm, 20 μm, and 12 μm diameter). The intermediate lens (with another deflector) and projector lens form the final image on a phosphor screen deposited on a fiber optic plate. This fiber optic plate scintillator serves also as the vacuum interface, and is directly coupled through a second fiber optic taper to a slow scan cooled CCD camera. This detector arrangement is about five times more efficient than a lens coupling of the camera.

The typical distance between the objective lens and the sample is 2 mm, and the maximum operating voltage is 30 kV. In practice most samples show the onset of considerable field emission at extraction voltages of 20–25 kV. This emission deteriorates the stability of the image and limits operation to lower voltages. The sample is held at high negative potential. The center electrodes of the lenses are biased to focus the electrons. All other electrodes and the detector are held at ground potential. The CCD camera can operate in two different modes with a maximum image acquisition rate of 4 images/s. This rate is sufficient for focusing and adjustment of the microscope. The camera accommodates variable exposure times, with typical image acquisition times of a few to tens of seconds.

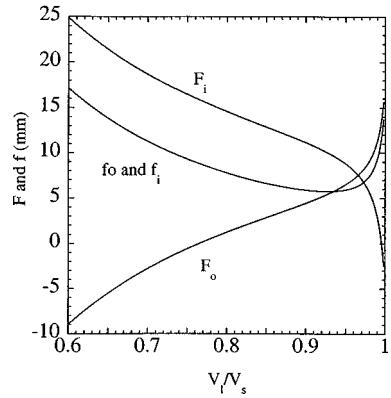

FIG. 2. Gaussian focal properties of the objective lens as a function of the lens voltage V_l to the sample voltage V_s. F_o, F_i and f_o, f_i are the object side and image side focal point and focal length, respectively. F_o, and F_i are measured from the sample position.

III. PEEM2 ELECTRON OPTICAL PROPERTIES

The electron optical components of PEEM2 are similar to Rempfer and co-workers[3] and Watts and co-workers[8] designs consisting of an asymmetric objective lens[42] and symmetric, unipotential, transfer, intermediate, and projector lenses.[43] The lens properties were calculated using custom developed internal electron optical codes and SIMION 6.0.[44] SIMION is a 3D ray tracing program solving the Laplace equation for a given electrostatic or magnetic electrode arrangement by finite differences (over-relaxation) and traces the trajectories of electrons or ions with defined starting conditions through the electron optical system. Figure 2 shows the Gaussian focal properties of the objective lens as a function of the voltage ratio between the lens (V_l) and the sample (V_s). F_o, F_i and f_o, f_i are the object side and image side focal points and focal lengths, respectively. F_o and F_i are measured from the sample position which we define as $z=0$. The properties of the objective lens were calculated in the absence of the accelerating field. Since image formation in PEEM has been described in detail elsewhere,[4,8] we mention it only briefly here. The accelerating field forms a virtual image of the object with unity magnification at a distance of $2l$ $(z=-l)$ from the objective lens where l is the distance between the sample and the first electrode of the objective lens. The chromatic aberrations of this accelerating field will be shown to limit the resolution of the microscope. The first electrode of the objective lens acts as an aperture lens for which the virtual image formed by the accelerating field is a virtual specimen. It is a weak (diverging) lens with the focal length of $-4l$[4,8] and forms another virtual image. The magnification is 2/3 and the image is located at $-1/3l$, i.e., behind the true specimen position. This is the object for the objective lens. The objective lens is operated at $V/V_s=0.775$ and forms an image at $z=150$ mm, this is the object for the transfer lens.

Figure 3 shows the image/object side (symmetric lens) Gaussian focal properties of the transfer/intermediate/projector lenses as a function of the lens voltage (V_l) to the sample voltage (V_s), F_i is measured with respect to the center of these lenses. For symmetric lenses, $f_o=f_i$ and $F_o=-F_i$. A transfer lens was added to the electron optics to

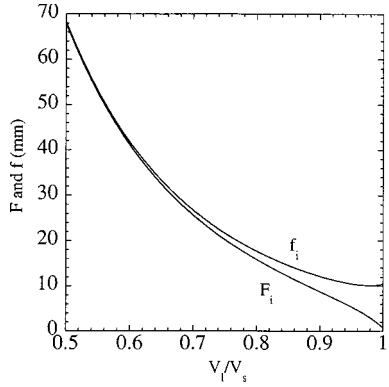

FIG. 3. Gaussian focal properties of the transfer/intermediate/projector lens as a function of the lens voltage V_l to the sample voltage V_s. For this lens $f_o = f_i$ and $F_o = -F_i$. F_o, F_i and f_o, f_i are the object side and image side focal point and focal length, respectively. F_o and F_i are measured from the lens center.

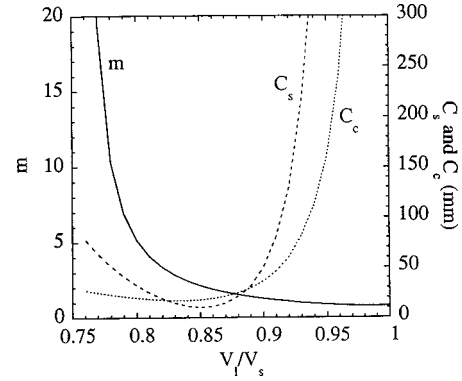

FIG. 4. Object side coefficients of spherical (C_s) and chromatic (C_c) aberrations and magnification m for the objective lens as a function of ration of lens voltage V_l to sample voltage V_s. The sample distance was fixed to 2 mm.

form an additional back focal plane where an angle limiting aperture is located, since a stigmator/deflector assembly is located in the (true) back focal plane of the objective lens. The transfer lens must be operated at a voltage so that the image of the back focal plane is outside the lens. From the lens dimensions and the lens properties (Fig. 3) we selected a distance of 32.5 mm from the lens center for the aperture location ($V/V_s = 0.66$). The transfer lens is located at $z = 215$ mm, the image formed by the objective lens at $z = 150$ mm is the object for the transfer lens that forms a unity magnification image at $z = 280$ mm. This image can be further magnified by either the intermediate lens (located at $z = 290$ mm) for lower magnification, or both the intermediate and projector lens (located at $z = 425$ mm) for higher magnification. This final image is at $z = 575$ mm.

The resolution of our x-ray excited PEEM is limited by the chromatic and spherical aberrations of the accelerating field and the lenses, and by diffraction at the aperture. It has been shown[4,8] for small apertures that diffraction limits the resolution. For larger apertures and UV produced threshold secondary electrons, the aberrations of the accelerating field and the lenses are comparable. For x-ray emitted electrons, the chromatic aberration of the accelerating field limits the resolution. The total spherical (C_s) and chromatic (C_c) aberration coefficients (referred to the object space) of a system consisting of n electron optical elements are calculated by [45]

$$C_s = (C_s)_1 + \frac{(C_s)_2}{m_1^4} + \frac{(C_s)_3}{m_1^4 m_2^4} + \frac{(C_s)_4}{m_1^4 m_2^4 m_3^4} +, \tag{1}$$

$$C_c = (C_c)_1 + \frac{(C_c)_2}{m_1^2} + \frac{(C_c)_3}{m_1^2 m_2^2} + \frac{(C_c)_4}{m_1^2 m_2^2 m_3^2} +, \tag{2}$$

where $(C_s)_n$ and $(C_c)_n$ are the spherical and chromatic aberration coefficients of the nth element and m_n is the magnification of the nth element. For PEEM2, $n = 1$ is attributed to the accelerating field, $n = 2$ to the aperture lens/objective lens system (this can be treated as one unit since the aperture lens hardly contributes to the aberrations[8]), $n = 3$ is the transfer lens, etc. The first two terms in Eqs. (1) and (2) are large since $m_1 = 1$, but all other terms are small because $m_2 = m_{\mathrm{ap}} m_{\mathrm{ob}} \approx 10$ with the magnification of the aperture lens $m_{\mathrm{ap}} = 2/3$ and the magnification of the objective lens $m_{\mathrm{ob}} \approx 15$.

The aberrations of the accelerating field can be estimated from an analytical calculation assuming a homogeneous field between sample and the first electrode of the objective lens (i.e., assuming that the aperture in the first electrode of the objective lens does not distort the electrical field significantly). The chromatic aberrations originate from the energy spread of the emitted electrons whereas the spherical aberrations are caused by the angular spread. If x rays are used for the illumination of the sample the energy distribution of the secondary electrons $n_e(E)$ can be approximated by $n_e \sim E/(E + W_f)^4$ (Ref. 46) while the number of the emitted secondary electrons is proportional to the cosine of the angle with respect to the surface normal.[47] E is the emission energy of the electron and W_f is the work function of the sample material. The transverse displacement of an object point Δr_{acc} caused by chromatic and spherical aberrations of the accelerating field is given by Refs. 4 and 8.

$$\Delta r_{\mathrm{acc}} = \frac{2l}{V_s} (\sqrt{E_p} - \sqrt{E} \cos \alpha_e) \sqrt{E} \sin \alpha_e, \tag{3}$$

where E_p is the peak of the emission energy distribution [typically $E_p = 1/3 W_f$ (Ref. 45)], and α_e is the electron take-off angle. The other relevant aberrations are those of the objective lens. Figure 4 shows the object space aberration coefficients C_s and C_c and the magnification of the objective lens as a function of V_l/V_s, and Fig. 5 shows the object space coefficients C_s and C_c of the transfer/intermediate/projector lens as a function V_l/V_s for infinite magnification. They were calculated applying the method of perturbed characteristic functions.[45,48] For the objective lens operated at a magnification of about 15, the aberration coefficients are $C_s = 60$ mm and $C_c = 25$ mm. They contribute to the total transverse displacement of an object point Δr_{ob} as[4,8]

$$\Delta r_{\mathrm{ob}} = \left(\frac{3}{2}\right)^4 C_s \left(\frac{E}{V_s}\right)^{3/2} (\sin \alpha_e)^3 - \left(\frac{3}{2}\right)^2 C_c \left(\frac{E - E_p}{V_s}\right) \sqrt{\frac{E}{V_s}} \sin \alpha_e. \tag{4}$$

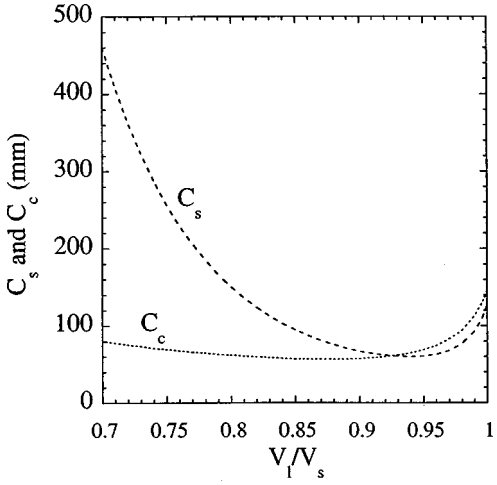

FIG. 5. Object side coefficients of spherical (C_s) and chromatic (C_c) aberrations for the transfer/intermediate/projector lens as a function of ration of lens voltage V_l to sample voltage V_s for infinite magnification.

The theoretical resolution limit of PEEM2 was calculated by taking the complete angular and energy distribution of the photoexcited secondary electrons into account. Only those electrons which are emitted at an angle α_e and an energy E that obey the condition [Eq. (5)] are transmitted through the microscope:[8]

$$E \leqslant \left(\frac{d m_{\mathrm{obj}} m_{\mathrm{acc}}}{2(f_i^{\mathrm{trans}})} \right)^2 \frac{V_s}{\sin^2 \alpha_e}. \tag{5}$$

Here d is the aperture diameter, f_i^{trans} the image side focal length of the transfer lens, m_{obj} and m_{acc} the magnification of the objective lens ($m_{\mathrm{obj}} \approx 15$), and of the accelerating field ($m_{\mathrm{acc}} = 2/3$). Our condition Eq. (5) is slightly different from that derived by Watts *et al.*[8] since our aperture is located behind the transfer lens and not the objective lens. Figure 6 shows the energy distribution of the transmitted electrons for various aperture diameters, for a sample voltage of 20 kV and $W_f = 4$ eV. While the energy distribution is narrowed by the aperture, it is still much wider than the energy distribution produced by threshold UV which can have an energy spread as low as 0.1 eV using monochromatization of the light. This is the reason for the higher spatial resolution of PEEMs operated using UV radiation [theoretically 5 nm, obtained so far about 10 nm (Ref. 4)] in comparison to PEEMs operated using x rays. The theoretical resolution limit considering all relevant aberrations is shown in Fig. 7 for different operation voltages of the microscope, and the transmission is shown in Fig. 8, both again for $W_f = 4$ eV. The highest resolution of 10 nm can be obtained using an aperture of 5 μm diameter and a sample voltage of 30 kV. The transmission for such a small aperture is around 1%. All these values depend on the work function of the sample material. Figure 9 shows the individual contributions of the diffraction at the aperture, the accelerating field, and the chromatic and spherical aberrations of all lenses. It demonstrates that the resolution of a PEEM using x rays is dominated by the aberrations of the accelerating field.

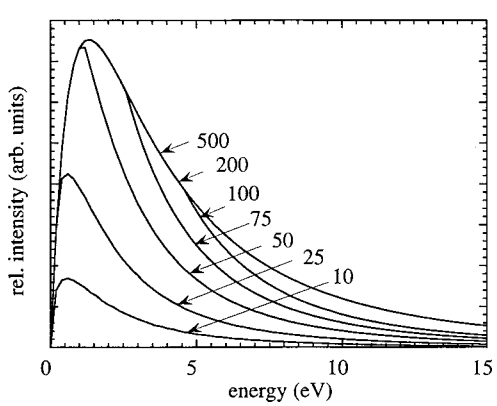

FIG. 6. Energy distribution of electrons transmitted through PEEM2 using apertures of different diameters (in μm) and a sample voltage of 20 kV; $W_f = 4$ eV.

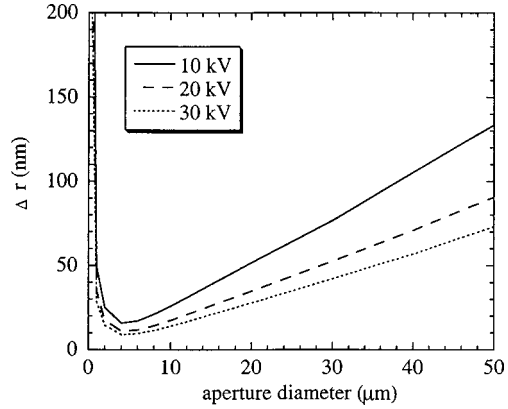

FIG. 7. The theoretical resolution limit considering all relevant aberrations for different operation voltages of the microscope; $W_f = 4$ eV.

IV. CONSTRUCTION OF THE PEEM2 END STATION

PEEM2 is installed at an angle of 55° with respect to the horizontal, and parallel to the beamline. This angle derives from the incidence angle of the x rays to the sample surface of 30° and the angle of the beamline with the respect to the horizontal of 5°. We have chosen this orientation of the microscope (in contrast to a horizontal arrangement) to be able to image samples with maximum linear in-plane polarization contrast. Figure 10 shows a drawing of the microscope. The lenses are mounted in a V block and held in position by clamps to assure the alignment of the lenses and enable an

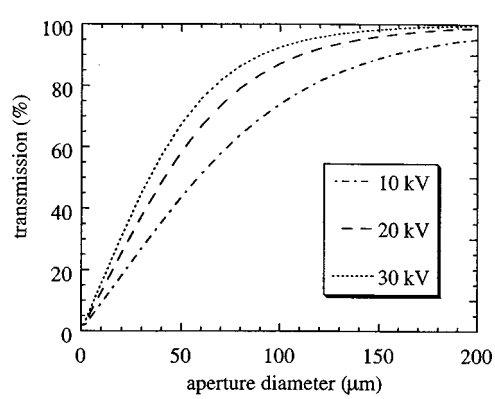

FIG. 8. Transmission of the microscope as a function of the aperture diameter for various operation voltages; $W_f = 4$ eV.

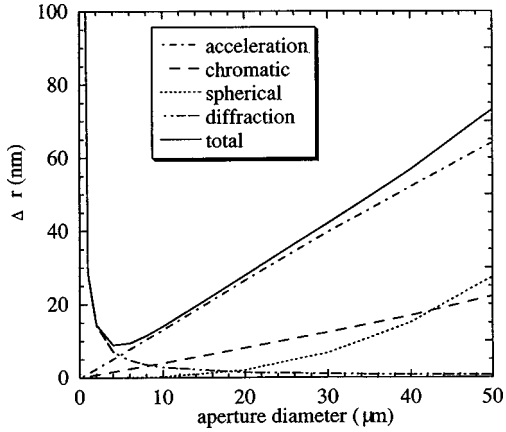

FIG. 9. Contributions of the various aberrations to the total resolution limit of PEEM2. Sample voltage 30 kV, $W_f = 4$ eV.

easy exchange of individual elements. The V block is mounted on a common massive flange with the sample manipulator for maximum stability, and is decoupled for vibration isolation from the rest of the vacuum vessel by welded bellows.

The lens electrodes are made from silicon aluminum bronze material that is easy to machine and to polish. Only the first electrode of the objective lens is made from titanium that does not have the tendency to grow whiskers during high voltage breakdown. This electrode has the highest probability to be exposed to electric breakdowns that occur occasionally between the lens and the sample. All electrodes were polished to a mirror finish, the alumina ceramic insulators were prebaked in vacuum, and the lenses were conditioned for high voltage breakdown stability by applying increasingly high voltages over a period of several days. The computer-controlled lens power supplies are current limited (0.1 mA) to avoid lens damage caused by breakdowns, they have a low ripple of 10^{-5} for stable microscope operation. It was calculated that a ripple of 3×10^{-4} causes image instabilities comparable to the theoretical resolution limit of the microscope. The microscope is mounted on a vibration isolated platform and is decoupled from vibrations of the beamline by a welded bellows. The high mechanical stability of the system allows acquiring local NEXAFS spectra averaged over areas as small as 100 nm with high energy resolution and reasonable signal-to-noise ratio. The resolution for local NEXAFS spectra is lower than the resolution for imaging because the acquisition of one image takes typically tens of seconds while the acquisition of a spectrum requires imaging at every energy step leading to typical spectra acquisition times of 10–20 min.

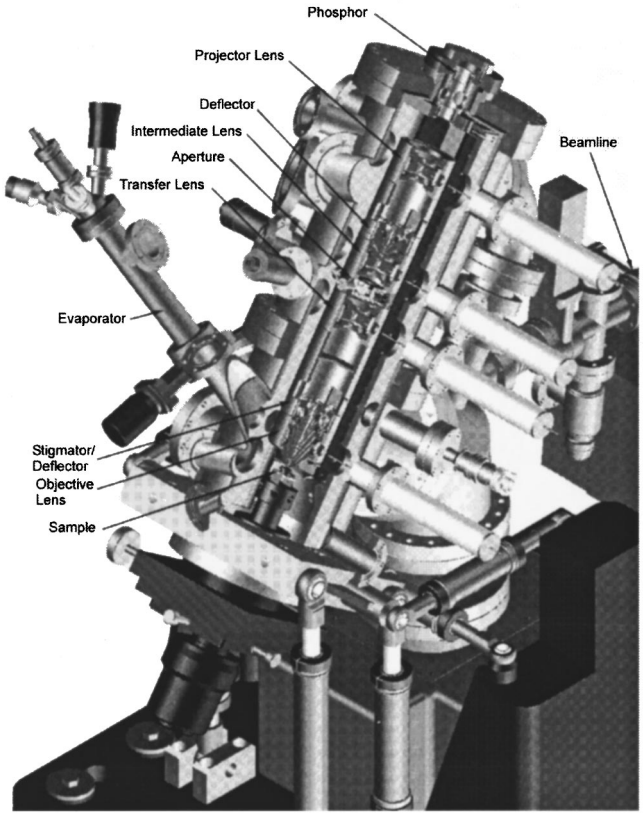

FIG. 10. Layout of PEEM2.

PEEM2 is equipped with a motorized, fast sample transfer system. The load lock chamber has a three sample parking stage. The sample preparation chamber includes a sputter gun, a LEED system, several evaporators, a quartz crystal film thickness monitor, a magnet (1000 Oe), and a movable sample stage that contains a heater and a shutter for multilayer and wedge structure growth. The microscope sample stage is retractable and the x-ray beam can be transmitted through the microscope vacuum vessel into a chamber downstream PEEM2 that contains a setup for XMCD spectroscopy (without spatial resolution) in alternating magnetic fields up to 750 Oe. This chamber is used for reference NEXAFS and XMCD measurements.

V. EXPERIMENTAL RESOLUTION TEST AND FIRST RESULTS

PEEM2 has been fully operational since summer 1998. Most of the experiments have been dedicated to the study of magnetic materials.[49,50] Here we demonstrate the spatial resolution of PEEM2 and show selected results on the study of magnetic nanostructures. The theoretical resolution limit can only be approached with a sample that fulfills conditions which were assumed for the calculation of the resolution. Many ''real world'' samples do not fulfill these conditions, and the resolution achieved with a PEEM will always vary with the sample properties. The ideal sample is highly conductive, very smooth, and has two different elements present at the surface with a very sharp interface and a very large difference in secondary yield (at least at some wavelength). Samples that are used for the testing of scanning electron microscopes prepared by nanofabrication techniques are not well suited to test the PEEM resolution because they typically have a certain surface topography that deteriorates the resolution of a PEEM. The best samples we have found to date are highly polished grainy materials, and (as a positive side effect of the undesired electrical breakdowns between objective lens and sample) tracks of surface discharges on insulating materials. Figure 11 shows a low resolution and a high resolution image of such a discharge track on a $LaFeO_3$

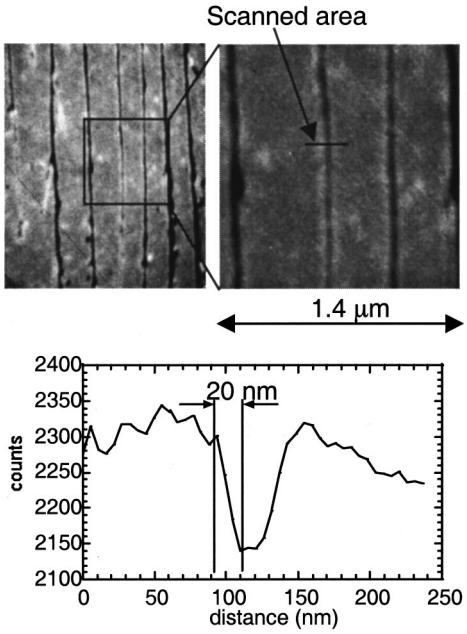

FIG. 11. Low resolution and a high resolution PEEM image of a discharge track on a $LaFeO_3$ sample acquired at the La M_5 edge. Estimated spatial resolution 20 nm.

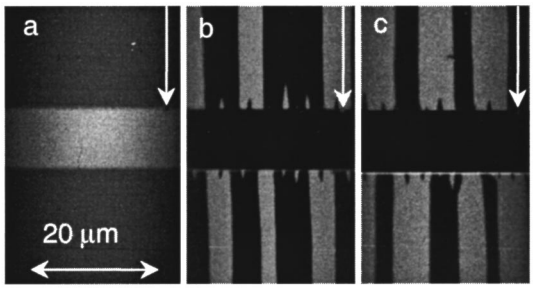

FIG. 12. (a) Image of nanofabricated Fe stripes acquired below the Fe L_2 and L_3 absorption edges at 710 eV. The Fe stripes are visible as broad dark stripes on the top and the bottom. (b) Difference image between images acquired at the Fe L_2 and L_3 absorption edges showing the magnetic domains in the stripes. Images acquired at room temperature; (c) same as (b) but images acquired at a temperature of 200 °C after heating the sample for 1 h. Arrows indicate the same defect on sample.

sample acquired at the La M_5 edge. The operation voltage was 23 kV, the 12 μm aperture was used, the exposure time was 60 s, and the estimated resolution is 20 nm. This is very close to the theoretical limit of the microscope for this aperture size and operating voltage (Fig. 7).

Magnetic imaging presents a greater challenge because the contrast based on the XMCD effect is typically only on the order of 5%–30% whereas it can be up to factors of 5–10 for elemental contrast. As an example we show XMCD images acquired of Fe wires fabricated[51,52] by first UHV *e*-beam evaporation and then patterning by optical contact lithography and ion milling. The wires consisted of highly epitaxial (110) oriented bcc-Fe grown on sapphire substrate with 100 nm molybdenum spacer layer to prevent charging. The Fe wires display a large in-plane uniaxial magnetocrystalline anisotropy with the easy axis parallel to the [100] direction, and perpendicular to the wire length. The Fe wires studied with PEEM2 had variable widths between 2 and 40 μm, spacings of 10–20 μm, about 3 mm length and thickness of 100 nm.[53] They were capped with either 1 or 6 nm of aluminum to prevent oxidation of the Fe. Local NEXAFS spectra obtained using PEEM2 showed that the 6 nm cap layer of Al prevented the oxidation of the Fe while the 1 nm cap layer did not completely protect the Fe which was slightly oxidized in this case. Figure 12(a) shows an image acquired below the Fe L_2 and L_3 absorption edges at 710 eV. The Fe stripes are visible as dark broad stripes on the top and the bottom because below the Fe absorption edge the secondary electron yield from the Fe is low. Magnetic PEEM images were obtained by taking a difference between the images acquired at the Fe L_3 and Fe L_2 absorption edges. The operating voltage was 20 kV, the 12 μm aperture was used, and the exposure time was 4 s at the L_3 edge and 8 s at the L_2 edge. Circularly polarized radiation was used with the photon beam direction perpendicular to the wire length. The arrows point to the same defect on the sample that was used to ensure that the same area on the sample was imaged. Magnetic PEEM images clearly show that the Fe(110) wires brake into stripe-like magnetic patterns with two alternating types of magnetic domains with domain magnetization direction being parallel or antiparallel to the [110] direction, as expected due to strong magnetocrystaline anisotropy.[51,52] For Fe wires with larger widths (10 μm and more) larger, metastable magnetic domains were observed, stabilized by spike domains at the wire edges as seen in the images in Figs. 12(b) and 12(c). We observed instantaneous change in the magnetic structures of such metastable domains with increased sample temperature. Figure 12(b) was acquired at room temperature, Fig. 12(c) at a temperature of 200 °C, both taken of the same sample area. It can be seen that the domain structure is significantly modified by the heating process. Experiments like this take advantage of PEEM being a full-field image technique that permits the real-time monitoring of magnetic domain structures.

Despite the low contrast in XMCD imaging the highest resolution we have achieved so far for magnetic imaging is better than 30 nm. This result was obtained on stripe domains in microfabricated Co wires.

This resolution for imaging using x rays is comparable to the best other instruments in the world and close to the theoretical limit for x-ray operation. A resolution of 22 nm was obtained by Schmidt and co-workers using a PEEM with an energy filter,[54] and 20 nm resolution was obtained using a PEEM without energy filter but with nonmonochromatized radiation.[55] PEEMs without energy filter and using monochromatized radiation typically have lower spatial resolution [75 nm,[8] 130 nm (Ref. 56)]. The resolution one obtains with a given PEEM depends on the sample, and good sample preparation and selection is crucial. Important for x-ray operated PEEMs is also the brightness of the x-ray source. PEEMs with very good electron optics that can be tested with UV light achieve only moderate resolution on second generation light sources because of the low signal-to-noise ratio. Better resolution can only be obtained by correcting for the aberrations of the microscope. The most promising approach to an aberration corrected PEEM seems to be the

application of an electrostatic mirror that requires the incorporation of a deflecting magnet into the PEEM design.[57–62] Aberration corrected PEEMs with energy filtering (small aperture or energy filter) might achieve a spatial resolution in the few nanometer range.[62] Operated with large apertures and no energy filter they will have a transmission close to 100% and at the same time a rather high resolution of about 30 nm. The high transmission will not only reduce the exposure time and thus help to improve the signal-to-noise ratio and the resolution, it will also drastically reduce the sample radiation damage in comparison to noncorrected PEEMs, and the study of radiation sensitive samples such as polymers will greatly benefit from this increased transmission. Aberration corrected PEEMs will enable spectromicroscopy in whole new dimensions by combining true nanoscale imaging capability with the full spectroscopic power of NEXAFS.

ACKNOWLEDGMENTS

Many people have contributed to the development of PEEM2. We would like to thank in particular Gertrude Rempfer, O. Hayes Griffith, and Ernst Bauer for many helpful suggestions and advice, Aline Cossy and Javier Diaz for their support in the early phase of the project, the excellent technicians at the ALS (Gregory Morrison, Dennis Gibson, and Michael De Cool) for their superb work in assembling the instrument, and Susanna Jacobsen, Jack Zelver, and Thomas Scarvie for their support in the software development. L.S. and B.S. would like to thank U. Ruediger, J. Yu, T. Kim, A, D. Kent, of New York University, for microfabricating the Fe-wire samples. This work was supported by the U.S. Department of Energy, Office of Basic Energy Sciences, under Contract No. DE-AC03-76SF00098. The work of L.S. and B.S. was supported by DARPA-ONR Grant No. N00014-96-1-1207.

[1] E. Brüche, Z. Phys. **86**, 448 (1933).
[2] O. H. Griffith and W. Engel, Ultramicroscopy **36**, 1 (1991).
[3] G. F. Rempfer, W. P. Skoczylas, and O. H. Griffith, Ultramicroscopy **36**, 196 (1991).
[4] G. F. Rempfer and O. H. Griffith, Ultramicroscopy **27**, 273 (1989).
[5] E. Bauer, Rep. Prog. Phys. **57**, 895 (1994).
[6] B. P. Tonner, G. R. Harp, S. F. Koranda, and J. Zhang, Rev. Sci. Instrum. **63**, 564 (1992).
[7] B. P. Tonner, D. Dunham, T. Droubay, J. Kikuma, J. Denliger, E. Rotenberg, and A. Warwick, J. Electron Spectrosc. Relat. Phenom. **75**, 309 (1995).
[8] R. N. Watts, S. Liang, Z. H. Levine, T. B. Lucatorto, F. Polack, and M. R. Scheinfein, Rev. Sci. Instrum. **68**, 3464 (1997).
[9] G. De Stasio, M. Capozi, G. F. Lorusso, P. A. Baudat, T. C. Droubay, P. Perfetti, G. Margaritondo, and B. P. Tonner, Rev. Sci. Instrum. **69**, 2062 (1998).
[10] R. M. Tromp and M. C. Reuter, Ultramicroscopy **36**, 99 (1991).
[11] W. Engel, M. E. Kordesch, H. H. Rothermund, S. Kubala, and A. von Oertzen, Ultramicroscopy **36**, 148 (1991).
[12] E. L. Montei, V. W. Ballarotto, M. E. Little, and M. E. Kordesch, J. Electron Spectrosc. Relat. Phenom. **84**, 129 (1997).
[13] J. Stöhr, *NEXAFS Spectroscopy* (Springer, New York, 1992).
[14] Y. Hwu, J. Electron Spectrosc. Relat. Phenom. **84**, 149 (1997).
[15] T. Droubay, G. Mursky, and B. P. Tonner, J. Electron Spectrosc. Relat. Phenom. **84**, 159 (1997).
[16] G. De Stasio and G. Margaritondo, J. Electron Spectrosc. Relat. Phenom. **84**, 137 (1997).
[17] S. Singh, H. Solak, N. Krasnoperov, F. Cerrina, A. Cossy, J. Diaz, J. Stöhr, and M. Samant, Appl. Phys. Lett. **71**, 55 (1997).
[18] S. Anders, T. Stammler, W. Fong, C.-Y. Chen, D. B. Bogy, C. S. Bhatia, and J. Stöhr, J. Tribol. (to be published).
[19] S. Anders, T. Stammler, W. Fong, D. B. Bogy, C. S. Bhatia, and J. Stöhr, J. Vac. Sci. Technol. (to be published).
[20] H. Ade, D. A. Winesett, A. P. Smith, S. Anders, T. Stammler, C. Heske, D. Slep, M. H. Rafailovich, J. Sokolov, and J. Stöhr, Appl. Phys. Lett. **73**, 3775 (1998).
[21] M. Samant, J. Stöhr, H. R. Brown, T. P. Russel, J. M. Sands, and S. K. Kumar, Macromolecules **29**, 8334 (1996).
[22] A. P. Smith and H. Ade, Appl. Phys. Lett. **69**, 3833 (1996).
[23] J. Stöhr, M. Samant, A. Cossy-Favre, J. Diaz, Y. Momoi, S. Odahara, and T. Nagata, Macromolecules **31**, 1942 (1998).
[24] A. Cossy-Favre, J. Diaz, Y. Liu, H. R. Brown, M. G. Samant, J. Stöhr, A. J. Hanna, S. Anders, and T. P. Russel, Macromolecules **31**, 4957 (1998).
[25] J. Stöhr, H. A. Padmore, S. Anders, T. Stammler, and M. R. Scheinfein, Surf. Rev. Lett. **5**, 1297 (1998).
[26] B. T. Thole, P. Carra, F. Sette, and G. van der Laan, Phys. Rev. Lett. **68**, 1943 (1992).
[27] J. Stöhr and H. König, Phys. Rev. Lett. **75**, 3748 (1995).
[28] B. P. Tonner, D. Dunham, J. Zang, W. L. O'Brien, M. Samant, D. Weller, B. D. Hermsmeier, and J. Stöhr, Nucl. Instrum. Methods Phys. Res. A **347**, 142 (1994).
[29] J. Stöhr, Y. Wu, B. D. Hermsmeier, M. G. Samant, G. R. Harp, S. Koranda, D. Dunham, and B. P. Tonner, Science **259**, 658 (1993).
[30] C. M. Schneider, R. Frömter, C. Ziethen, W. Swiech, N. B. Brookes, G. Schönhense, and J. Kirschner, Mater. Res. Soc. Symp. Proc. **475**, 381 (1997).
[31] D. Spanke, V. Solinus, D. Knabben, F. U. Hillebrecht, F. Ciccacci, L. Gregoratti, and M. Marsi, Phys. Rev. B **58**, 5201 (1998).
[32] W. Rave and A. Hubert, IEEE Trans. Magn. **26**, 2813 (1990).
[33] B. Petek, P. L. Trouilloud, and B. E. Argyle, IEEE Trans. Magn. **26**, 1328 (1990).
[34] T. J. Silva, S. Schultz, and D. Weller, Appl. Phys. Lett. **65**, 658 (1994).
[35] R. Schad, S. M. Jordan, M. J. P. Stoelinga, M. W. J. Prins, R. H. M. Groeneveld, and H. W. van Kesteren, Appl. Phys. Lett. **73**, 2669 (1998).
[36] J. N. Chapman, A. B. Johnston, L. J. Heyderman, S. McVitie, W. A. P. Nicholson, and B. Bormans, IEEE Trans. Magn. **30**, 4479 (1994).
[37] J. Unguris, R. J. Celotta, and D. T. Pierce, J. Appl. Phys. **75**, 6437 (1994).
[38] H. Poppa, E. Bauer, and H. Pinkvos, MRS Bull. **20**, 38 (1995).
[39] D. Rugar, H. J. Mamin, P. Guenther, S. E. Lambert, J. E. Stern, I. McFadyen, and T. Yogi, J. Appl. Phys. **68**, 1169 (1990).
[40] H. J. Hug, B. Stiefel, P. J. A. van Schendel, A. Moser, R. Hofer, S. Martin, H.-J. Güntherodt, S. Porthun, L. Abelmann, J. C. Lodder, G. Bochi, and R. C. O'Handley, J. Appl. Phys. **83**, 5609 (1998).
[41] H. A. Padmore, M. R. Howells, and W. R. McKinney, in *Techniques of Vacuum Ultraviolet Physics*, edited by J. A. Samson and D. A. Ederer (Academic, Orlando, FL, 1997).
[42] G. H. N. Riddle, J. Vac. Sci. Technol. **15**, 857 (1978).
[43] G. Rempfer, J. Appl. Phys. **57**, 2385 (1985).
[44] D. A. Dahl, J. E. Delmore, and A. D. Appelhans, Rev. Sci. Instrum. **61**, 607 (1990) for an earlier version of the program, see http://www.pesinc.com/~pesinc/simiondos.html for the latest version.
[45] M. Szilagyi, *Electron and Ion Optics* (Plenum, New York, 1988), Chap. 5-5.
[46] B. Tonner and D. Dunham, Nucl. Instrum. Methods Phys. Res. A **347**, 436 (1994).
[47] B. L. Henke, J. Liesegang, and S. D. Smith, Phys. Rev. B **19**, 3004 (1979).
[48] P. A. Sturrock, *Static and Dynamic Electron Optics* (Cambridge University Press, Cambridge, 1955).
[49] S. Anders, H. Padmore, A. Scholl, J. Stöhr, J. Lüning, L. Séve, B. Sinkovic, and M. Scheinfein, Spring Meeting of the Materials Research Society, San Francisco, April 1999.
[50] S. Anders, H. Padmore, A. Scholl, J. Stöhr, J. Lüning, and M. Scheinfein, 1999 Meeting of the American Physical Society, Atlanta.
[51] U. Ruediger, J. Yu, S. Zhang, A, D. Kent, and S. S. P. Parkin, Phys. Rev. Lett. **80**, 5639 (1998).
[52] U. Ruediger, J. Yu, A. D. Kent, and S. S. P. Parkin, Appl. Phys. Lett. **73**, 1298 (1998).
[53] L. Séve, B. Sinkovic, S. Anders, A. Scholl, H. Padmore, U. Ruediger, J. Yu, T. Kim, and A. D. Kent, Appl. Phys. Lett. (to be published).
[54] Th. Schmidt, S. Henn, B. Ressel, K.C. Prince, and E. Bauer, VIth International Conference on X-ray Microscopy, Berkeley, CA, August 1999.
[55] G. De Stasio, L. Perfetti, B. Gilbert, O. Fauchoux, M. Capozi, P. Perfetti, G. Margaritondo, and B. P. Tonner, Rev. Sci. Instrum. **70**, 1740 (1999).

[56] C. Ziethen, O. Schmidt, G. H. Fecher, C. M. Schneider, G. Schönhense, R. Fromter, M. Seider, K. Grzelakowsi, M. Mertel, D. Funnemann, W. Swiech, H. Gundlach, and J. Kirschner, J. Electron Spectrosc. Relat. Phenom. **88**, 983 (1998).
[57] G. Rempfer, J. Appl. Phys. **67**, 6027 (1990).
[58] G. F. Rempfer and M. S. Mauck, Optik (Stuttgart) **92**, 3 (1992).
[59] Z. Shao and X. D. Wu, Optik (Stuttgart) **84**, 51 (1990).
[60] Z. Shao and X. D. Wu, Rev. Sci. Instrum. **61**, 1230 (1990).
[61] Z. Shao and X. D. Wu, Appl. Phys. Lett. **55**, 2696 (1989).
[62] R. Fink, M. R. Weiss, E. Umbach, D. Preikszas, H. Rose, R. Spehr, P. Hartel, W. Engel, R. Degenhardt, R. Wichtendahl, H. Kuhlenbeck, W. Erlebach, K. Ihmann, R. Schlögl, H.-J. Freund, A. M. Bradshaw, G. Lilienkamp, Th. Schmidt, E. Bauer, and G. Brenner, J. Electron Spectrosc. Relat. Phenom. **84**, 231 (1997).